CFD EVALUATION OF A 3RD GENERATION LDI COMBUSTOR

Kumud Ajmani
Vantage Partners, LLC
Cleveland, Ohio, USA

Hukam Mongia
CSTI Associates, LLC
Yardley, PA, USA

Phil Lee
Woodward FST, Inc
Zeeland, MI, USA

1.0 ABSTRACT

The National Combustion Code (NCC) was used to perform non-reacting and two-phase reacting flow CFD analysis of a nineteen-element injector array for a third-generation (N+3) Lean-Direct Injection (LDI) combustor. The nineteen injection elements were configured into a three-module, 7-5-7 element configuration. The air passages of the pilot and main injection elements consisted of CFD-optimized compound-angle discrete jets and dual axial-bladed swirl-venturi passages, respectively. The pilot and main injection elements were fueled with conventional pressure-atomizers and fuel-filming nozzles, respectively. The aerodynamic characteristics of the nineteen-element injection array were evaluated by performing non-reacting flow simulation using a Time-Filtered Navier-Stokes (TFNS) method. Fuel-air mixing and combustion performance was evaluated with reacting-flow TFNS computations using a 14-species, 18-step reduced kinetics mechanism for Jet-A fuel, lagrangian spray modeling and a PDF turbulent-chemistry interaction model. The TFNS reacting-flow simulations provided considerable insight into the correlation between aerodynamics, combustion and emissions performance of the newly-designed pilot and main elements of the LDI-3 combustor at simulated cruise conditions.

2.0 INTRODUCTION

The ever-increasing emphasis on reducing fuel consumption and CO2 emissions with attendant increase in engine operating pressures along with lowered CO and NOx emissions and proposed reductions in particulate emissions are providing incentive for the redesign of lean-dome combustor technologies. NASA Glenn Research Center (GRC) has invested considerable experimental and computational resources over the past two decades in the development of Lean Direct Injection (LDI) technology for aircraft engine combustors [Tacina 2005][1]. The Environmentally Responsible Aviation (ERA) program was very successful in meeting NASA's N+2 (2020-2025 time-frame) goals for combustor emissions reduction and performance at various engine cycle conditions [Van Zante 2015][2].

Some high-level overviews of the computational and experimental efforts performed for NASA's N+2 ERA program have been reported in [Walton 2015][3] and [Reddy 2016][4]. Highlights of experimental lean-dome combustor and injector redesign efforts performed for the ERA program were reported by [Goeke 2014][5] (Goodrich's radially staged multipoint LDI), [Hicks 2014][6] (UTRC's PICS injector), [He 2015][7] (Parker Hannifin's three-zone LDI concept), [Tacina 2016][8] (Woodward FST's axial-bladed swirl-venturi LDI concepts), [He 2016][9] (P&W's ACS Combustor), and [Herbon 2017][10] (GE's TAPS-II design). The CFD analysis to support the ERA programs LDI-2 injector designs used many of the best-practices developed for the NCC using single-element and nine-element LDI-1 designs [Ajmani 2013][11]. Details of the CFD efforts using NASA's NCC code for the ERA program's LDI-2 configurations were reported by [Ajmani 2014a][12] (Woodward FST's LDI-2) and [Ajmani 2014b][13] (Goodrich's multipoint LDI).

NASA's N+3 (2030-2035) program sets more stringent emissions and performance goals for propulsion systems for small-core engines [Ashcraft 2011][14], in addition to increased emphasis on design of fuel-flexible combustors [Hicks 2016][15], [Surgenor 2016][16]. Some details of a new multi-point LDI configuration (LDI-3) to meet NASA's N+3 goals, as proposed by Woodward FST, Inc. were described in [Ajmani 2016][17]. The new design is based on a combination of five-element and seven-element modules, arranged in an annular array within the combustor, and considerably simplifies the injector layout and fuel management as compared to Woodward's LDI-2 designs. A three–module design built by Woodward FST, consisting of nineteen injection elements (two 7-element modules surrounding a recessed 5-element

module) has recently been tested in NASA GRC's CE-5 flame-tube facility [Tacina 2017][18].

NCC has served as a useful tool to help screen LDI-3 fuel-filming injectors [Ajmani 2015][19] and provide CFD-based optimization [Ajmani 2016][17] of air-swirler designs for Woodward FST's LDI-3 configurations. A detailed analysis of the aerodynamic performance, fuel-air mixing and combustion characteristics of a five-element module (four mains, one pilot) of Woodward FST's LDI-3 design was reported in [Ajmani 2016][17]. The current work reports on a CFD evaluation with NCC of a nineteen-element LDI-3 flametube assembly derived from two seven-element injection modules (six mains, one pilot in each module), surrounding a central five-element injection module.

The goal of the current CFD analysis of the integrated, individual LDI-3 components and modules is (a) to provide CFD-based 'reacting flow-visualization' for the 19-element LDI-3 assembly, with potential insight into the interaction between the individual injectors of each module, and between the 7-element and 5-element injection modules, (b) to further refine the 'NCC best practices' framework for future, detailed comparisons of CFD predictions of LDI-3 emissions with measured experimental data, and (c) to identify CFD-informed potential improvements in the current LDI-3 flametube design for full-annular design and testing.

3.0 NCC COMPUTATIONAL SIMULATION METHODOLOGY

The NCC is a state-of-the-art computational tool that is capable of solving the time-dependent, Navier-Stokes equations with chemical reactions. The NCC is being developed primarily at the NASA GRC in order to support combustion simulations for a wide range of applications, and has been extensively validated and tested for low-speed chemically reacting flows. Several 'best practices' for the use of NCC for LDI injector design were achieved by extensive 'anchoring' [Ajmani 2013][11] with available LDI-1 data [Tacina 2005][1]. The anchoring work enabled the use of NCC in the evaluation of LDI-2 designs [Ajmani 2014a][12] and advanced CFD screening of LDI-3 designs [Ajmani 2016][17] at NASA GRC.

The NCC uses second-order accurate central-differences for the convective and diffusion flux discretization, and a Jameson operator (a blend of 2nd and 4th-order dissipation terms) for numerical stability. The second and fourth order dissipation parameters are typically set to 10^{-4} and 0.05, respectively [Swanson 1997][20]. The value of k_2, the constant that scales the second order dissipation gradient switch, is typically set to 0.25. In order to enhance convergence acceleration in pseudo-time, implicit residual smoothing is used to smooth the computed residuals in NCC RANS. Turbulence closure is obtained by using a two-equation, cubic k-ε model with variable Cμ ([Shih 1998][21]) and dynamic wall functions with pressure gradient effects ([Shih 2000][22]). Time-integration of the flow equations is performed by a steady-state RANS approach, or a time-accurate Time-Filtered Navier-Stokes/Very-Large Eddy-Simulation (TFNS) [Liu 2011][23] approach.

3.1 LDI-3 GEOMETRY, MESHING AND CFD SETUP

The National Combustor Code (NCC) was used to perform simulations of a nineteen-element flametube configuration of an LDI-3 combustor proposed by Woodward FST, Inc (WFST). The 19 elements are grouped in three modules, with a 7-5-7 element dome layout. Each module comprises of a central pilot-injector and four (or six) surrounding main-injection elements (see figure 1). The candidate LDI-3 arrangement with a minimally recessed 5-element central module is designated as the 'baseline' configuration for the CFD simulations reported in this paper. The venturi exits of the two 7-element modules are in-line with the combustor dome plate hot side.
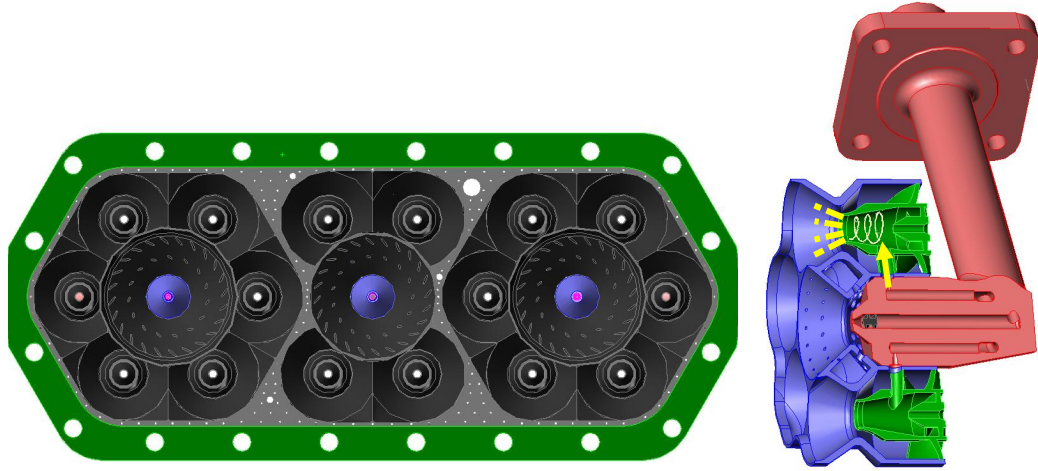
Figure 1. Dome-layout and CAD for a LDI-3 combustor with one five- and two seven-injection element arrays
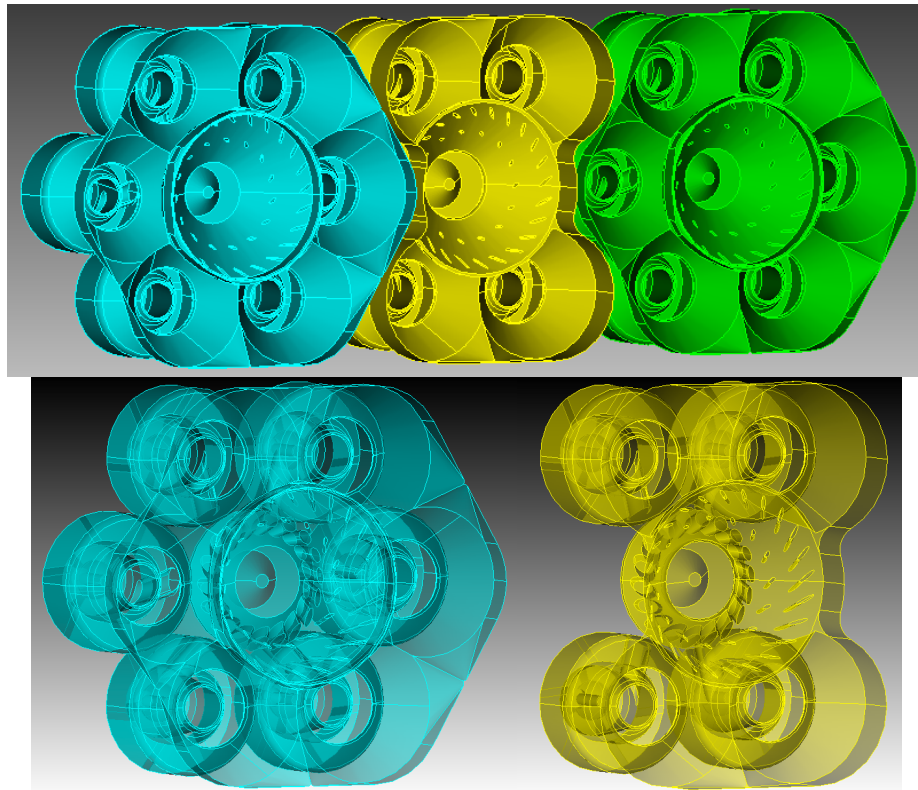

Figure 2. Dome-layout and CAD for a LDI-3 combustor with five- and seven-injection element arrays

A summary of the CFD-optimized LDI-3 geometry design parameters [Ajmani 2016][17] fabricated by Woodward FST, Inc. for flame-tube testing is given in the following paragraphs:

1. **Pilot Injector with axial fuel-injection**: Integrated multi-element injector with circumferential slots for air injection – 45% offset (w.r.t. axial centerline) for the pilot air-swirler inflow passages. All three pilots have a CW (clockwise) swirl when viewed from the downstream direction; refer to [Ajmani 2016][17] for details.

3

2. **Main Injectors with pre-filming fuel injection and axial bladed air swirlers**: Co-axial, counter-rotating, 48° outer (six blades) and 60° inner (four blades) axial venturi swirl-passages. In addition, each adjacent main injector reverses the swirl orientation of the outer air swirlters.w.r.t. the pilot swirlers.

The nineteen-element LDI-3 geometry consisting of a central 'five-element' module surrounded by two 'seven-element' modules CAD supplied by WFST (see figure 1) was imported into the CUBIT mesh-generation software (see cubit.sandia.gov), to create a fully tetrahedral mesh with 22M elements, see figure 3. Each blade passage and venturi was meshed as an individual block, and these blocks were then "imprinted" or merged with connecting volumes at their respective common surfaces. This ensured consistency of meshing across similar geometric elements, and also allowed for potential 'drop-in' replacement of the axial air swirlers for the main injectors, and/or the radial air-swirler for the pilot, without needing to regenerate the complete mesh for the entire configuration. Best-practices for meshing of axial-bladed venturi passages and the entrance and exit regions of individual injectors, as reported in [Ajmani 2013][11] were leveraged for the current LDI-3 meshing.
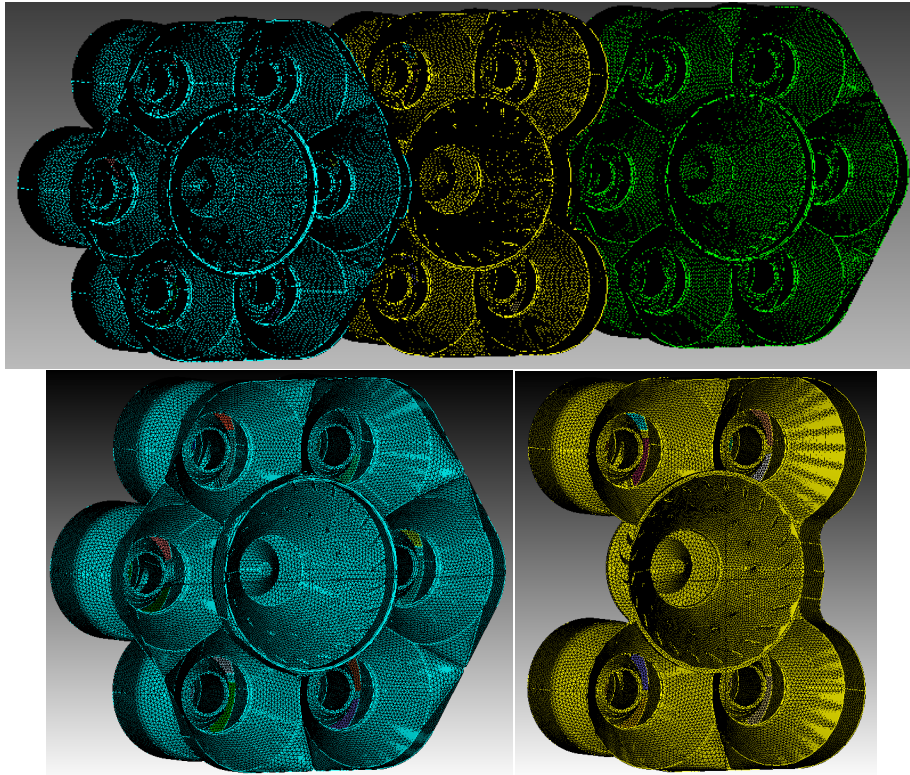
Figure 3. Surface Mesh for nineteen-element LDI-3 assembly (top); surface mesh for seven-element injector (bottom left) and five-element injector (bottom right) components

4.1 CFD Results: RANS Non-Reacting Flowfield

NCC RANS computations were performed for the 3rd generation LDI (LDI-3) combustor assembly. The non-reacting flow results were primarily used to perform a baseline comparison of effective-area prediction with measured experimental results. The initial conditions were based on inflow conditions of P_3=130psi, T_3=811K, and an overall 3% pressure drop (Δp). Adiabatic, no-slip boundary conditions were imposed at all solid walls. Fixed total-pressure (Pt_3) and total-temperature (Tt_3) conditions were imposed at all inflow faces (based on given P_3, T_3) for all the upstream boundaries (mains, pilots, cooling holes). The static pressure at the downstream outflow plane (P_4) was fixed at a value computed from the desired pressure drop (P_3-Δp). At convergence, the CFD computed mass-flow rate that satisfied the desired P_3, T_3 and ΔP was used to calculate the effective area (AC_d) of the various components (injectors, cooling holes) of the combustor assembly.

The non-reacting flow simulations consisted of NCC RANS computations until a 'mass-imbalance (outflow-inflow) convergence of 0.1% over 500 consecutive iterations was achieved. A total of 44,000 RANS iterations at a CFL of 0.95 were typically required to obtain a converged, steady-state, non-reacting flow solution. The CFD-predicted mass-flow rates at the inlet planes of the sixteen main injectors, the three pilot injectors and the various cooling holes, were used to compute the total AC_d of the nineteen-injector configuration. Two experimental values were reported: (a) the total AC_d in the flametube (19 elements, with cooling flows), and (b) the AC_d with the pilot injectors blocked off (16 elements, with cooling flows). The difference between (a) and (b) was reported as the AC_d for the pilots, and measurement (b) was reported as the AC_d for the mains. A comparison of the computed and experimentally measured AC_d values are shown in Table 1. The differences in the individual and total AC_d values between experiment and CFD were in the 6-8% range, which were within the pre-established acceptable 10% error margin. Note that the CFD analysis does compute estimates of the AC_d values for the cooling flows (pilot cooling rows, dome face cooling). These CFD estimates can be useful to determine the AC_d impact of adding (or subtracting) cooling holes in future injector designs.

Table 1. Effective area (AC_d) comparison of CFD computations (NCC RANS) and measured values (Woodward FST, Inc)

| Inflow Boundary	Computed Mass-Flow Rate (kg/s)	Computed AC_d (in^2)	Measured AC_d (in^2)	%Error
Main Injectors (16)	0.7139	2.4323	2.3613*	6.6%
Pilot Injectors (3)	0.0983	0.3348	0.3104	7.9%
Pilot Cooling Rows (6)	0.0127	0.0433	(included in Mains)	
Dome Face Cooling	0.0123	0.0418	(included in Mains)	
Total	**0.8372**	**2.8522**	**2.6717**	**6.8%**

Computed AC_d (CFD) = $mdot_{CFD}$ / sqrt (2 * ΔP * rho) (CFD used measured value of ΔP=26882Pa for AC_d computation)

Representative details of the injector assembly and the corresponding flow features in the various flow passages can be seen in the 3-D cross-sectional contour plot of axial velocity contours (figure 4). All the significant details of the assembly are successfully captured in the CFD meshing process, as validated by the AC_d comparison shown earlier. In addition, smaller features are also modeled, as seen by the reverse flow (light blue regions) seen behind the cooling holes that line the periphery of the combustor face. The representative airflow through the various axial-bladed swirlers for the mains, and the pilot injector passages can also be seen in the cutaway cross-section upstream of the combustor face shown in figure 4.
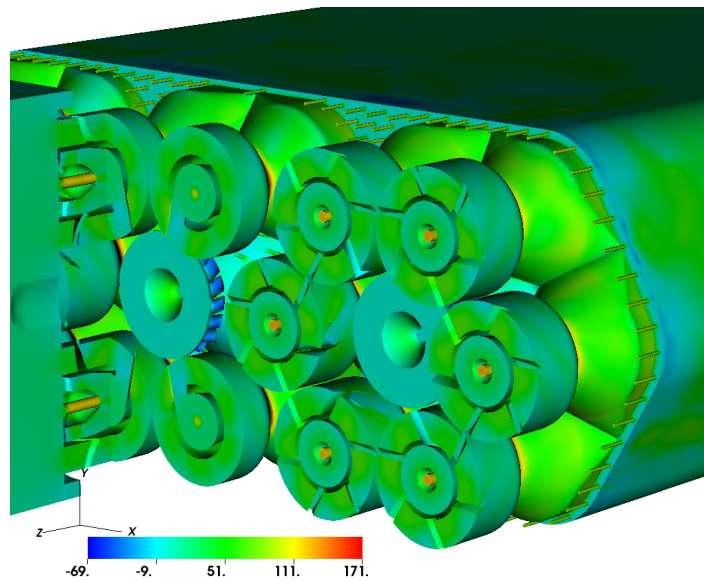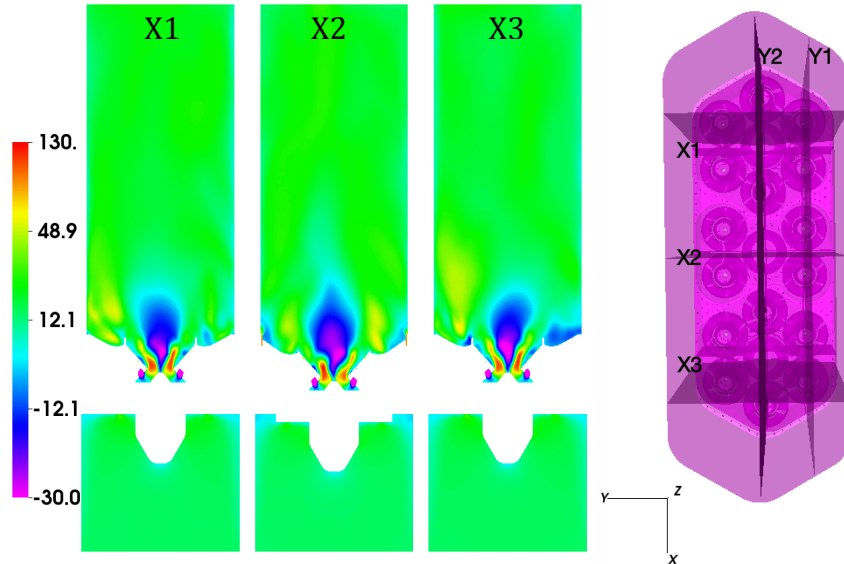

Figure 4. Contours of axial velocity (m/s) through the nineteen element LDI-3 combustor

5

Figure 5a shows axial velocity contours for the non-reacting flowfield in two axial mid-planes through the nineteen element LDI-3 assembly. The locations of the planar slices are shown in figure 5b. The Y-axis mid-plane (figure 5a, left, plane Y2) shows the flow through all the three pilots and four of the main elements in the 7-element modules. The Y-axis offset-plane (figure 5a, right, plane Y1) shows the flow through two main elements for each of the 7-element modules and the central 5-element module. Strong *central recirculation* (CTRZ) zones are present behind the three pilot elements, as seen in plane Y2 and all three X-axis planes (figure 5b). The CTRZ extends 30-35mm downstream of the fuel injection plane. In contrast, only weak *corner recirculation* (CORZ) zones are present along the walls of the diverging section of the venturi behind each of the main elements (planes Y1 and Y2). Note that the NCC RANS solution shows a noticeable lack of flow symmetry along the centerlines of the injector elements. This prediction of asymmetry for highly swirling flows is a typical characteristic of the RANS approach.
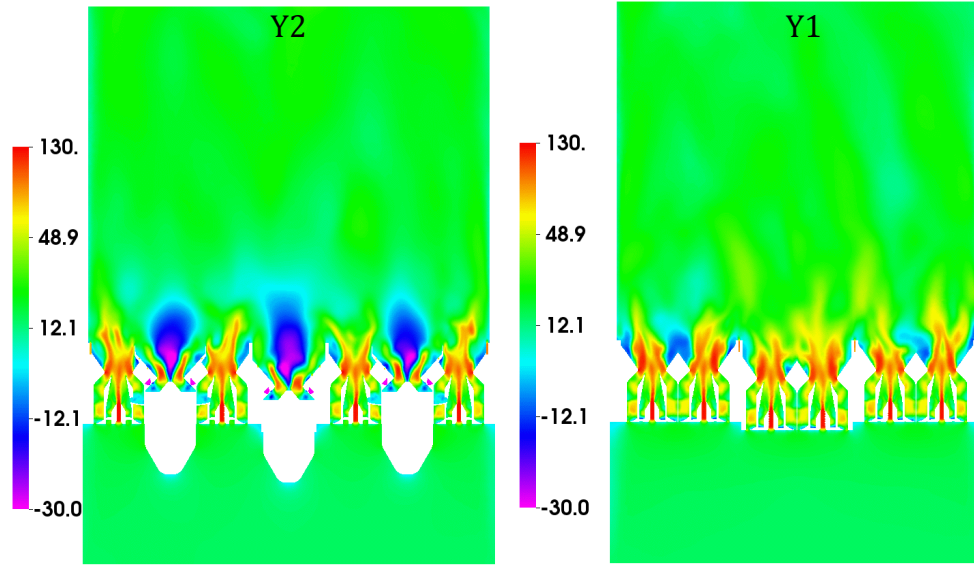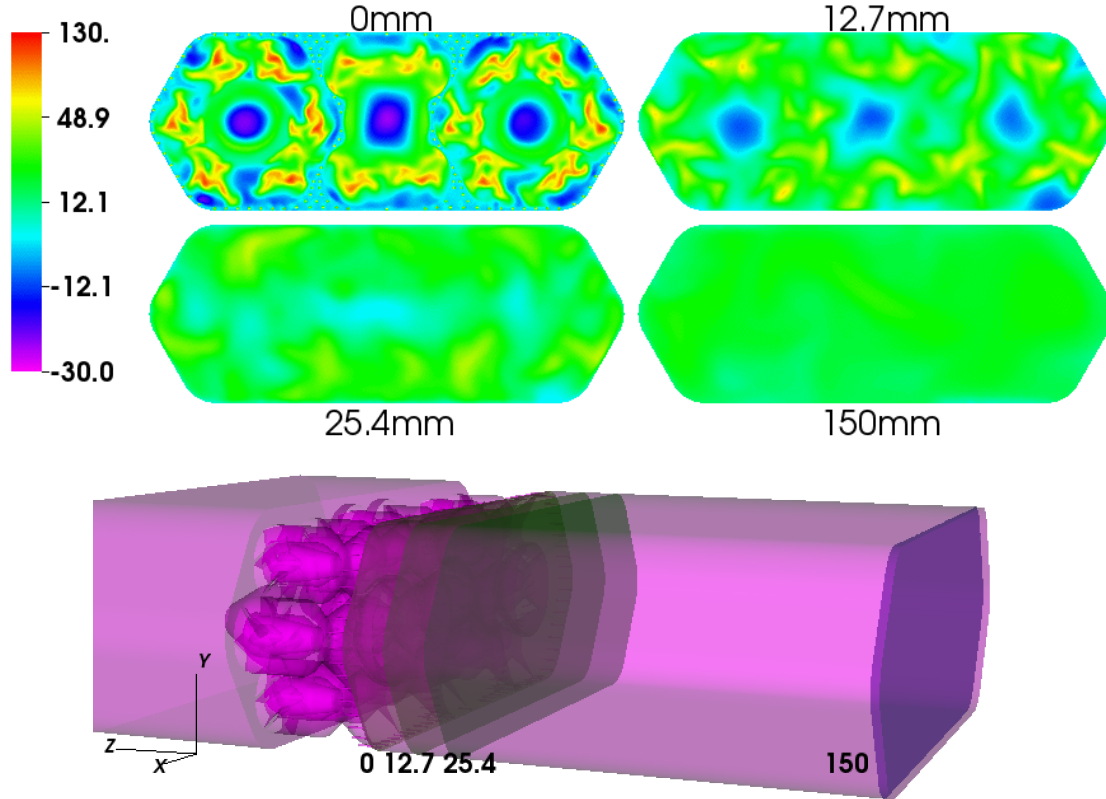

Figure 5a. Contours of axial velocity (m/s) (NCC **RANS Non-Reacting** flow): Axial slices at Y-axis planes (Y1, Y2) (top) and X-axis planes through three pilots (X1, X2, X3) (bottom).

Figure 5b. Contours of axial velocity (m/s) (NCC **TFNS Non-Reacting** flow): Axial slices at X-axis planes through the three pilots

Axial-velocity contours for four additional cross-sections along the length of the combustor are shown in figure 6. The combustor face is shown at the 0mm plane, and two additional planes near the face are shown at the 12.7mm (0.5") and 25.mm (1.0") axial locations. The 150mm plane downstream of the face represents the location of experimental measurements of emissions data. The 0mm plane shows the central recirculation zones (CTRZ) for the central pilots, and some scattered regions of recirculation generated by the swirlers for the main injection elements. The CTRZ behind central five-element module is marginally different from that created by the two outer seven-element modules due to its 4mm (0.15") recess from the dome. At 12.7mm, the CTRZ behind all three pilots is considerably weakened, and very little CTRZ remains in the flow at the 25.4mm location. The flow is fairly mixed out and uniform at the 150mm plane.

Figure 6. Contours of axial velocity (m/s) (NCC **RANS Non-Reacting** flow): Transverse cuts at combustor dome face (0mm), two downstream planes and exit plane (150mm); locations of transverse planes along combustor

In summary, the NCC RANS non-reacting analysis provides some limited insight into the flow-fields characteristics of the individual injector elements and their interactions with their neighbors. The main contribution of NCC RANS is in providing a quick estimate of the effective area prediction and comparison with experimental AC_d measurements. The NCC RANS AC_d predictions are used as a measure of meshing-fidelity, and a computational metric to be satisfied before proceeding to the much greater computational effort required for the Time-Filtered Navier Stokes (TFNS) simulations.

4.2 CFD Results: NCC TFNS Non-Reacting Flowfield

The NCC RANS non-reacting flow predictions were used as an initial condition for the NCC Time-Filtered Navier-Stokes (TFNS) solver. The TFNS solver uses a time-accurate form of the Navier-Stokes equations with dual time-stepping and time-filtering [Liu 2011][23]. The advantage of using a TFNS approach, as compared to an LES approach is that the relatively coarse RANS-like mesh can be used to obtain VLES-like fidelity. The TFNS uses a user-selected filtering control parameter (FCP) which is

compatible with the underlying mesh resolution, to determine the split between the portion of the large-scale turbulence that is directly computed and that which is modeled with traditional turbulence modeling. An FCP value of 0.51 is used for all computations reported in this work.

Figures 7a and 7b shows the axial velocity contours for the non-reacting NCC TFNS solution in several planes through the nineteen-element injector assembly. The solution shown represents the mean flow averaged over 17500 time-steps (17.5m-s), i.e. three flow-through times for the computational domain. For the three pilot elements, NCC TFNS shows central recirculation zones that are at least 50% longer and wider (plane Y2, planes X1, X2, X3) as compared to the NCC RANS solution (figures 5a, 5b). In addition, each of the main injectors show very distinct central recirculation zones (plane Y1) with the NCC TFNS approach, as compared to the NCC RANS solution which predicted no central recirculation. The NCC TFNS solution (plane Y1) also shows a complete absence of the weak corner recirculation zones adjacent along the main venturi walls, as compared to the NCC RANS solution. Note that NCC TFNS is able to predict much better expected symmetry of the flow and the recirculation zones along the centerlines of the injection modules, in contrast to NCC RANS which is unable to capture very few flow symmetry characteristics. Future planned diagnostics of one of the seven-element modules of the nineteen-element assembly at NASA GRC's CE-13 facility will help validate some of the non-reacting NCC TFNS results.

Figure 8 shows the axial velocity contours for the non-reacting NCC TFNS solution in four cross-sections along the combustor length. The individual central recirculation zones behind each injector are much more well-defined at the 0mm plane, as compared to NCC RANS (figure 6). In addition, the pilot recirculation zones exist beyond the 25.4mm plane for NCC TFNS, which suggests a longer mixing region as compared to NCC RANS. NCC TFNS does indicate that the non-reacting flow is very well mixed out at the experimental emissions probe location of 150mm.
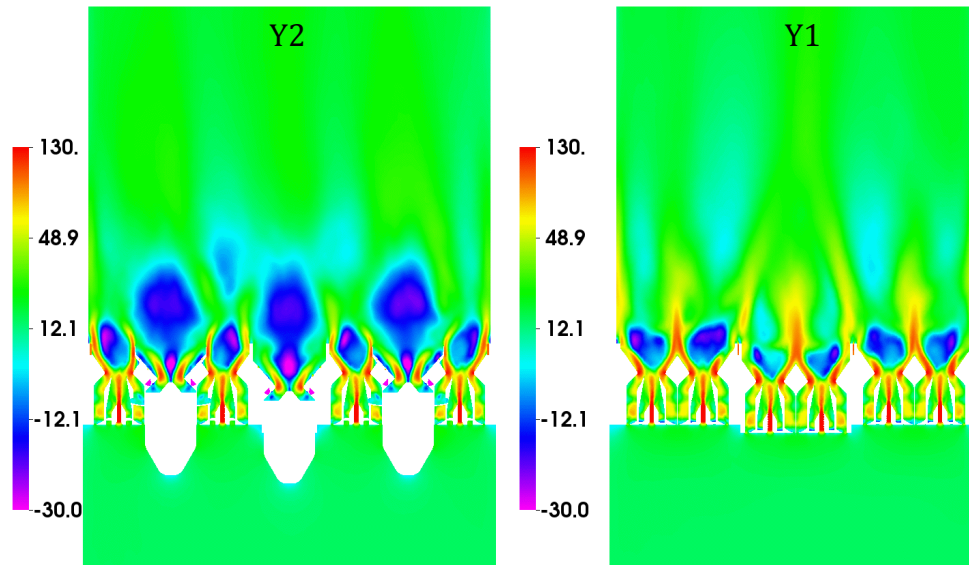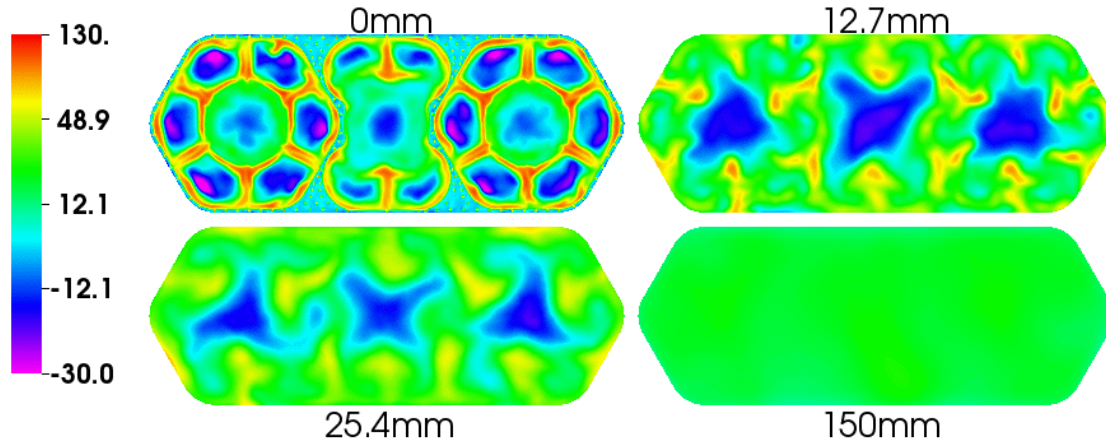

Figure 7a. Contours of axial velocity (m/s) (NCC **TFNS Non-Reacting** flow): Axial cut at Y-axis mid-plane (left, three pilots and four mains) and Y-axis quarter-plane (right, six mains)
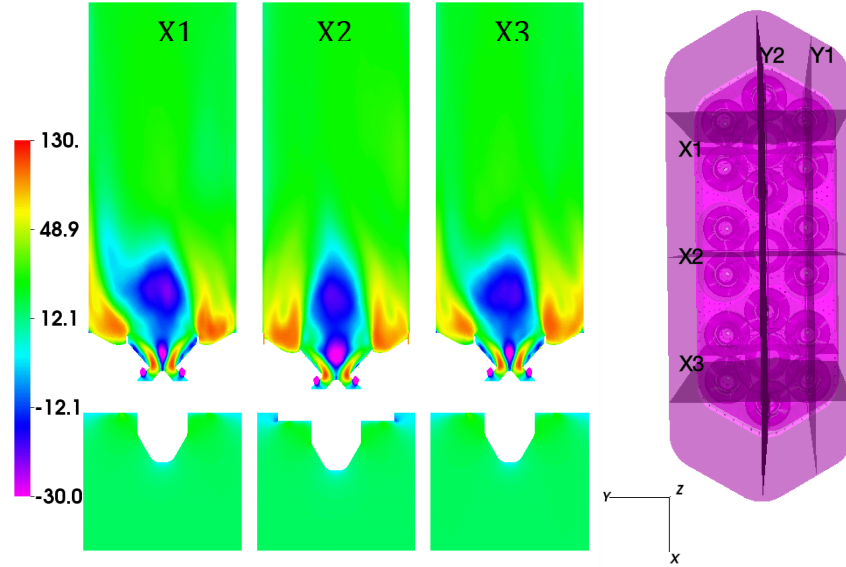
Figure 7b. Contours of axial velocity (m/s) (NCC **TFNS Non-Reacting** flow): Axial slices at X-axis planes through the three pilots (X1 and X3 for 7-element modules, X2 for 5-element module)

Figure 8. Contours of axial velocity (m/s) (NCC **TFNS Non-Reacting** flow): Transverse cuts at combustor dome face (0mm), two downstream planes, exit plane (150mm)

Note that there are very minor differences between the predicted effective area of NCC RANS and NCC TFNS (see Table 2). However, the predicted flow structures are significantly different between the two methods. With NCC TFNS, the flow structures behind each pilot element are similar, as are the flow features behind each main element. In addition, a more consistent, symmetric flow-field across similar injector components is predicted by NCC TFNS. In view of this, the remainder of this paper will focus on reporting NCC TFNS results for predictions of fuel-air mixing behavior and emissions performance with reduced-chemistry reacting-flow computations.

Table 2. NCC RANS compared to NCC TFNS: effective area (AC_d) prediction

Effective Area (AC_d)	Total (in^2)	Mains + Cooling (in^2)	Pilot (in^2)
Experiment	2.6717	2.3613	0.3104
NCC CFD (RANS)	2.8522	2.5174	0.3348
NCC CFD (TFNS)	2.7377	2.3915	0.3462

Computed AC_d (CFD) = $mdot_{CFD}$ / sqrt (2 * ΔP * rho) (CFD used measured value of ΔP=26882Pa for AC_d computation)

4.3 NCC TFNS Reacting Flowfield Predictions

In this section, reacting flow results for a representative N+3 cycle condition at a 'high-power' ICAO point are presented. The flow conditions evaluated correspond to engine cycle condition represented by P_3=130psi, 4% ΔP, T_3=1000F (811K) and FAR=0.03. The NCC TFNS solver is used with a reduced kinetics finite-rate chemistry model and Lagrangian spray-modeling for the liquid fuel. Turbulence-chemistry interaction is modeled with a PDF transport model [Liu 2014][24] using a joint-scalar Monte-Carlo method [Raju 2000][25]. The computational time for reacting-flow NCC TFNS with turbulence-chemistry interaction is 10x relative to non-reacting NCC TFNS on NAS Supercomputing's Pleiades Cluster using 1000 cores (ivy-bridge nodes). Each non-reacting TFNS cycle representing a single flow-through time-period through the domain requires 5x-7x the computational time of a typical non-reacting RANS solution.

Chemical Kinetics and Ignition Modeling

A computationall*e* kinetics mechanism (of fewer than 20 species) with liquid spray simulations of Jet-A fuel which can provide NOx and CO predictions, and lean blow-out, at high P_3, high T_3, and low equivalence ratio (< 0.5) conditions for LDI combustor design, remains an open challenge for the chemical kinetics community. In the current work, a 14-species, 18-reactions reduced-kinetics model was used to compute the species source-terms for Jet-A/air combustion using finite-rate (see Appendix A). Jet-A fuel is modeled as a surrogate mixture of decane (73%), benzene (18%) and hexane (9%). The kinetics mechanism was validated by matching adiabatic flame temperature, flame-speed and ignition-delay with experimental shock-tube data and LDI-1 emissions data, in the equivalence ratio range of 0.5 to 1.0 [Ajmani 2014c][26]. The mechanism used for the current LDI-3 analysis was also validated against LDI-2 experimental emissions data [Ajmani 2014a][12].

The CFD simulation was typically ignited by introducing artificial ignition source terms in a 1mm wide region, 2mm downstream of each individual venturi-exit plane. The ignition sources were turned off in the NCC when every computational cell in the ignition zone reached a 'cutoff' temperature of 1600K, or if 1000 iterations with the ignition sources were reached. No "re-ignition" of the mixture was allowed, once the NCC solver had turned off the ignition sources. This 'best practice' approach ensures consistency of computational ignition modeling when comparing the performance of different injector configurations and different operating (power/equivalence ratio) conditions of the combustor.

Liquid Phase and Spray Modeling

The liquid spray (Jet-A fuel) was modeled by tracking spray particles in a Lagrangian framework, where each particle represents a group of actual spray droplets [Raju 2012][27]. The governing equations for the liquid phase are based on a Lagrangian formulation where the spray particle position and velocity are described by a set of ordinary differential equations. The Lagrangian solution process used for this study employs a best-practice unsteady spray model such that droplet groups are only integrated for a fraction of their lifetime (but restarted at this point for the next iteration), rather than to a completely steady-state solution. The typical spray integration time-steps were 1e-7s (local time-step, *dtml*), and 1e-6s (global time-step, *dtgl*) which is also the gas-phase physical time-step. This translates to 10 local time-steps for each global time-step for the spray solver.

An inflow droplet size distribution is prescribed by the correlation equation:

$$\frac{dn}{n} = 4.21x10^6 \left[\frac{d}{d_{32}}\right]^{3.5} e^{-16.98\left(\frac{d}{d_{32}}\right)^{0.4}} \frac{dd}{d_{32}}$$

Here n is the total number of droplets, d_{32} is the Sauter mean diameter (SMD), and dn is the number of droplets in the size range between d and $d + dd$. A user-specified number of 'droplet groups' is used to represent the drop size distribution among a finite number of droplet classes.

The specification of the fuel injector exit condition plays a major role in the fidelity of the NCC simulations. Spray injection of fuel particles was specified 1mm downstream of the injector-exit plane of the simplex injectors (pilots). A droplet initial temperature of 300K, Sauter Mean Diameter (SMD),

d_{32}=9μm, and an injection velocity of 38m/s was specified based on measurements made by Woodward FST at atmospheric flow conditions. A 60° hollow cone spray with the annular angle width of 10^0 (viz. droplets spread within 55° to 65° region), 10 droplet groups discretized into 32 spatial streams along the 360^0 circumference was modeled. At each spray time-step, the droplet streams were permitted a stochastic variation of the stream location within the 10° cone thickness. As the typical SMD (d_{32}) was less than 10μm, the droplets were assumed to undergo evaporation without any secondary breakup.

For the filming injectors (mains), sixteen discrete fuel streams spread evenly at a location 1mm downstream of the each main injector's exit plane are used to simulate the fuel exiting the pre-filmer. Each of the sixteen discrete fuel streams for each injector is modeled as a 10^0 solid cone (10 droplet groups, 8 spatial streams, d_{32}=8μm, and injection velocity=5m/s). Details of the predicted droplet distribution of a single pre-filming injector with NCC TFNS are shown in figure 9. Most of the liquid fuel has evaporated immediately downstream of the dump plane, and the isometric view shows a fairly even distribution of fuel in the circumferential direction surrounding a relatively hollow center. The CFD prediction of droplet fuel distribution is qualitatively similar to the measured particle distribution (hollow center, even circumferential distribution) of Woodward FST shown in figure 9 (right).
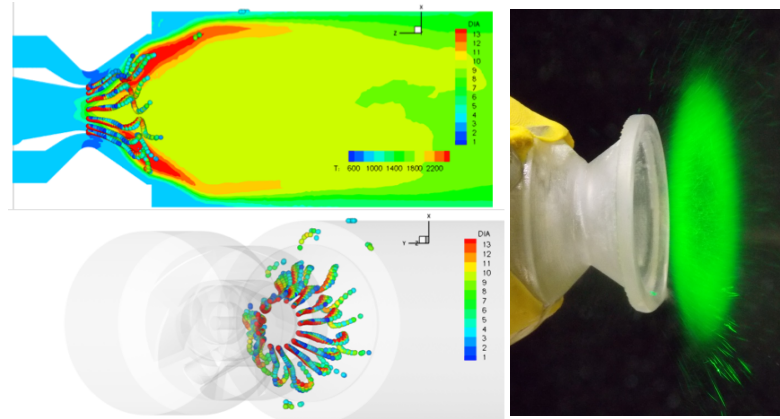

Figure 9. Left: Temperature (K) contours and predicted particle distribution for pre-filming injector (Time-averaged NCC TFNS reacting-flow) Right: Measured particle distribution (Woodward FST).

The 'PDF-like' model of NCC [Liu 2014][24] using 25 Monte-Carlo particles per grid element is used in conjunction with reduced-kinetics finite-rate chemistry to obtain the reacting flow TFNS solution. Figures 10a and 10b shows the axial velocity contours for the reacting NCC TFNS solution in several planes through the nineteen-element injector assembly. For the three pilot elements (planes X1, X2, X3), reacting flow NCC TFNS (figure 10a) shows central recirculation zones (CRZ) that are very different as compared to the non-reacting flow NCC TFNS solution (figure 7a). The mass recirculating in the CRZ zones behind the three pilots is computed to be 25% less than that for non-reacting flow. The thin CRZ regions behind the mains of the two 7-element modules (planes Y1 and Y2) are the result of long, axial shear layers (red 'fingers') that are formed on the interfaces between adjacent main injection elements.

Figure 11 shows the axial velocity contours for the reacting NCC TFNS solution in four cross-sections along the combustor length. The individual CRZs behind each injector are similar to that observed for non-reacting flow. As compared to non-reacting flow (figure 7), the pilot CRZ for the central 5-element module is smaller and more diffusive in nature than those for the two 7-element modules, particularly at the 12.7mm and 25.4mm planes. This behavior of the flow behind the pilot for the 5-element module results in a very different flame structure as compared to the flames behind the pilots of the 7-element modules.
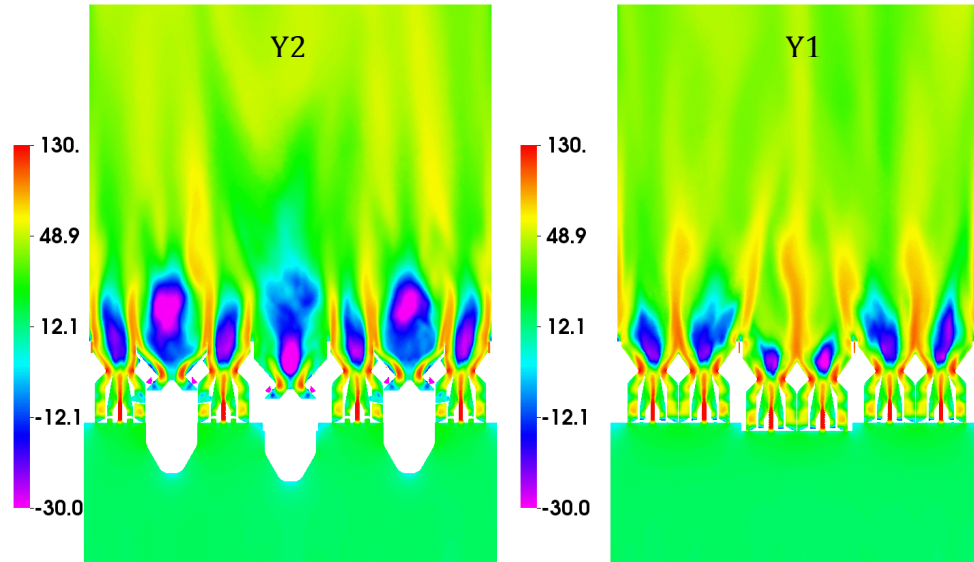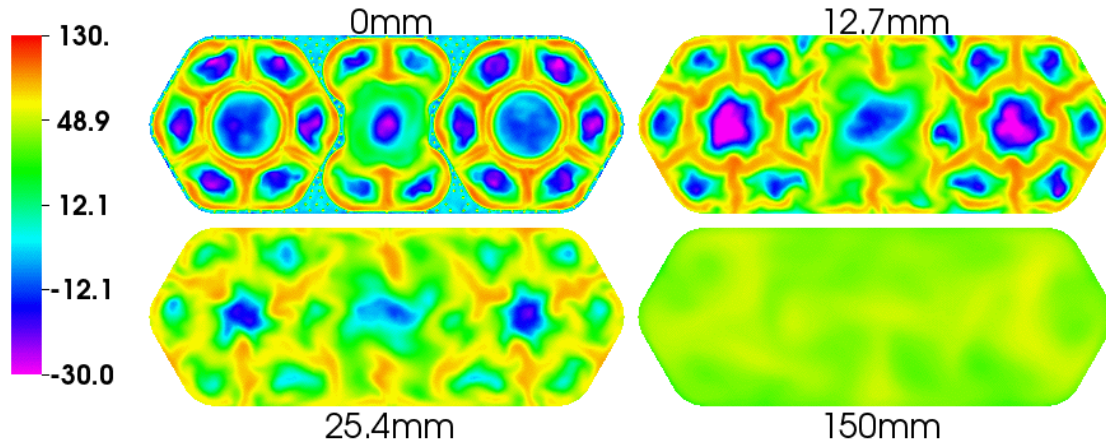
Figure 10a. Contours of axial velocity (m/s) (NCC **TFNS Reacting** flow): Axial cut at Y-axis mid-plane (left, three pilots and four mains) and Y-axis quarter-plane (right, six mains)
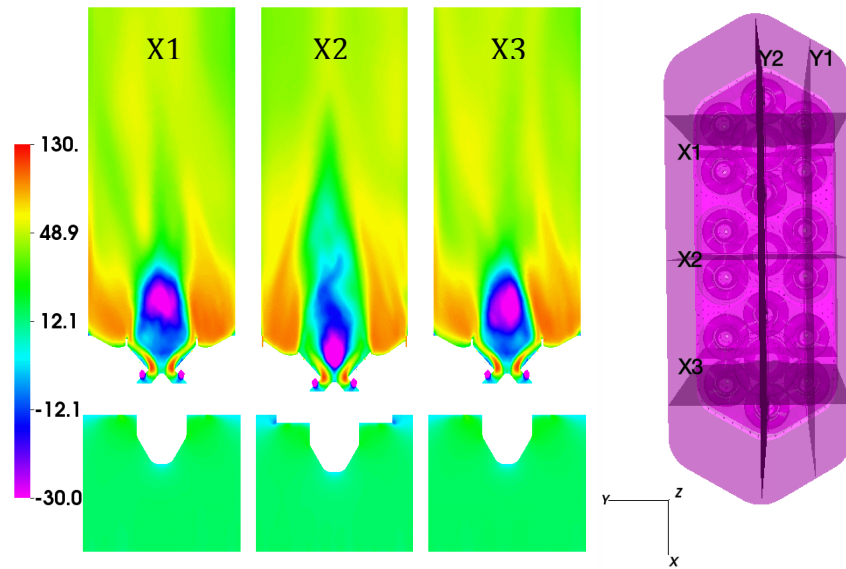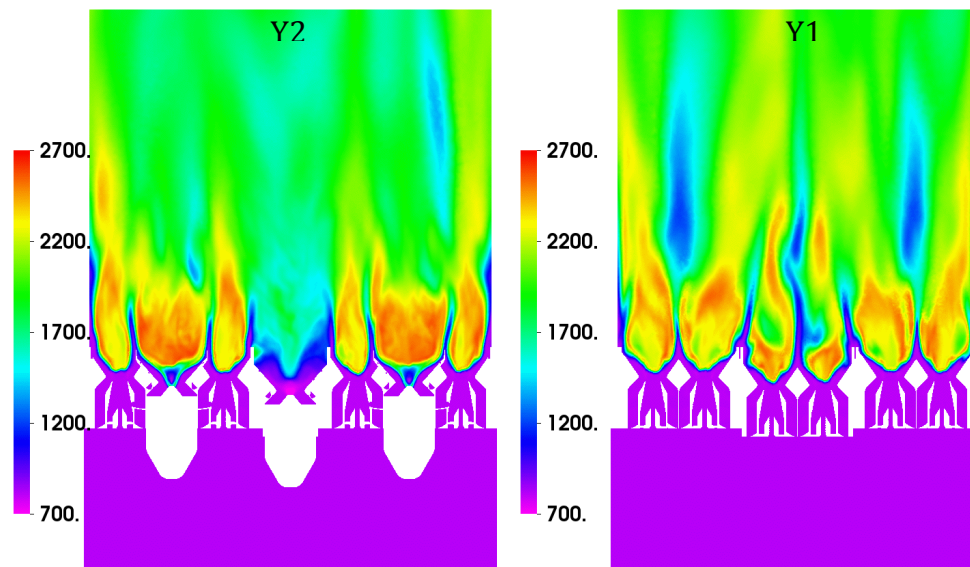

Figure 10b. Contours of axial velocity (m/s) (NCC **TFNS Reacting** flow): Axial slices at X-axis planes through the three pilots (X1 and X3 for 7-element modules, X2 for 5-element module)

Figure 11. Contours of axial velocity (m/s) (NCC **TFNS Reacting** flow): Transverse cuts at combustor dome face (0mm), two downstream planes, exit plane (150mm)

Figures 12a and 12b shows temperature contours for the reacting NCC TFNS solution in several axial planes. In plane Y1 (figure 12a, right), very distinct individual flame zones are predicted for each of the six main injectors shown. There are thin regions of relatively cold flow corresponding to the shear layers formed at the interfaces of the main injectors and the pilot injectors (figure 12a, plane Y1 and Y2). In figure 12b, a very distinct, strong hot wall/cold wall effect is predicted for the 7-element modules, which dissipates as the temperature gradients start to mix out towards the final third of the combustor length. For the five-element module pilot (plane X2 of figure 12b), cold flow near both the walls surrounds a relatively weak 'diffusion flame', and the temperature gradients start to mix out in the final half of the combustor.
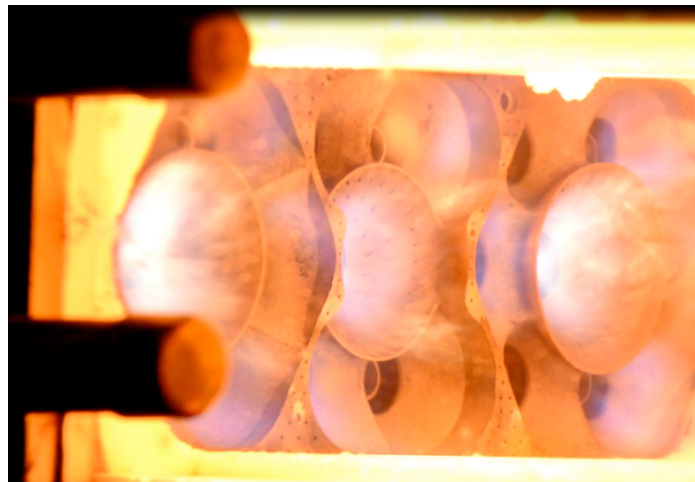

Figure 12a. Contours of temperature (K) (NCC **TFNS Reacting** flow): Axial cut at Y-axis mid-plane (left, three pilots and four mains) and Y-axis quarter-plane (right, six mains)

13
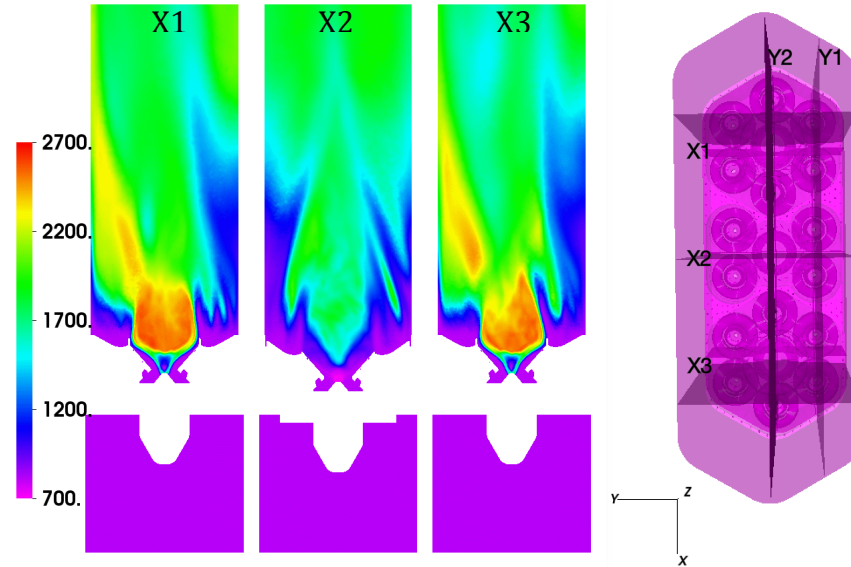
Figure 12b. Contours of temperature (K) (NCC **TFNS Reacting** flow): Axial slices at X-axis planes through the three pilots (X1 and X3 for 7-element modules, X2 for 5-element module)

A snapshot from a video taken at Woodward FST during reacting-flow experimental tests of the 19-element assembly is shown in figure 13. The flow conditions were P_3=131psia, T_3=1113F (874K), dP = 3%, pilot FAR=0.0288, mains FAR=0.0212, overall FAR=0.0233 (N+3 cycle, 100% ICAO). Note that the reacting flow NCC TFNS results presented here are for a slightly lower T_3=811K and a higher overall FAR=0.03 as the CFD was performed before the N+3 100% ICAO cycle conditions were finalized at NASA GRC. Transverse cross-sections of temperature contours shown in figure 14 can be used to qualitatively compare the flame-structure in the near dome-region (0mm, 12.7mm). Results shown in figures 12a and 12b may be used to compare the CFD and the experimental flames upstream of the dome face in the diverging sections of the pilot and main-injector venturis. There seems to be reasonable qualitative agreement between the CFD and the experiment for the flame structure, except for the prediction of the weak flame for the pilot element of the 5-element module.


Figure 13. Snapshot of reacting flow-field for 19-Element LDI-3 flametube (Woodward FST, Inc.)
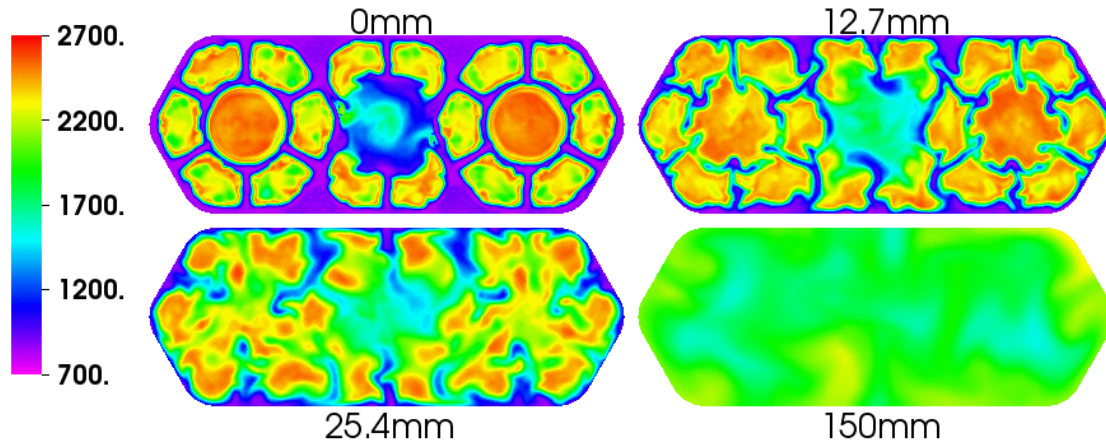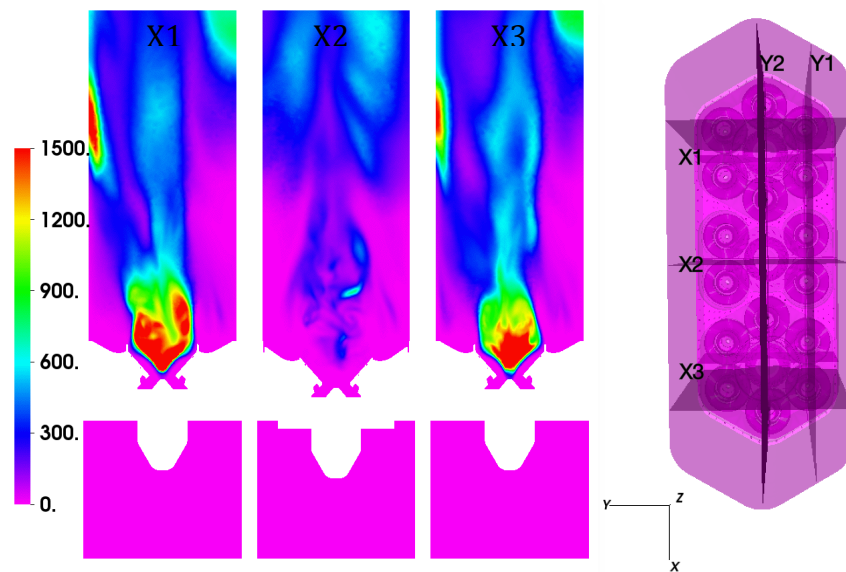
Figure 14. Contours of temperature (K) (NCC **TFNS Reacting** flow): Transverse cuts at combustor dome face (0mm), two downstream planes, exit plane (150mm)

One of the primary stated goals of NASA's N+3 design and development program is the reduction of LTO NOx to 80% below CAEP-6 standards for large engines with smaller cores. The current CFD analysis thus integrates the equations for NOx computations as part of the reduced-kinetics chemistry mechanism. This approach avoids the need for post-processing for NOx predictions, at the cost of additional CFD computational cost. The inclusion of three NOx species (NO, NO_2 and N_2O) and their reactions, takes into account both thermal and prompt NOx formation. As reported in the NCC TFNS validation study with the 5-element module [Ajmani 2016][17] of the 19-element studied here, this *in-situ* NOx computation approach coupled with PDF-like turbulence-chemistry interaction has a significant improvement on the accuracy of EINOx predictions when compared with experimental data.

Figures 15a and 15b show NCC TFNS predicted contours of NO mass-fraction at various axial planes. The majority of the NO seems to be produced immediately behind the pilot injectors of the 7-element modules (plane Y2 of figure 15a, planes X1 and X3 of figure 15b). A much lower intensity of NO formation happens immediately downstream of the throat of each main injector (plane Y1 of figure 15a). Some regions of high NO intensity are also seen in the latter half of the combustor. This NO formation happens in the downstream regions where the flames produced by the individual elements finally start to mix together. Figure 16 shows the very high NO production by the two 7-element pilots (0mm, 12.7mm planes), and almost negligible NO behind the very weak flame of the 5-element pilot. The 150mm plane shows very high non-uniformity in the NO profile, which is a result of the peaks in the NO production in the latter half of the combustor (figures 15a and 15b). Quantitative comparisons of predicted EINOx values of the 19-element LDI-3 flametube assembly will be reported in a future paper after planned experimental tests at NASA GRC's CE-5 facility. The CE-5 tests will report on performance and emissions of Woodward's LDI-3 for 7%, 30% and 100% ICAO engine power conditions [Tacina 2017][18].
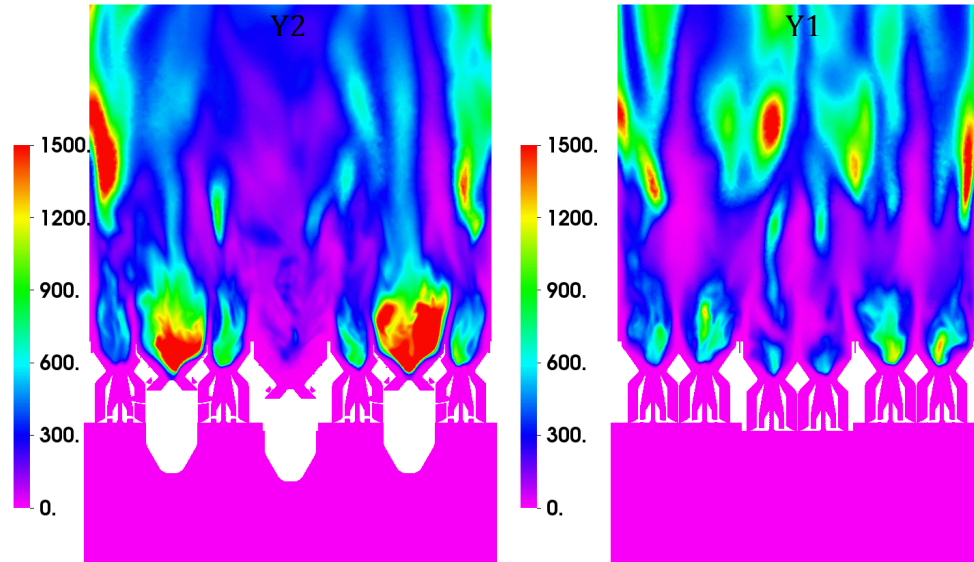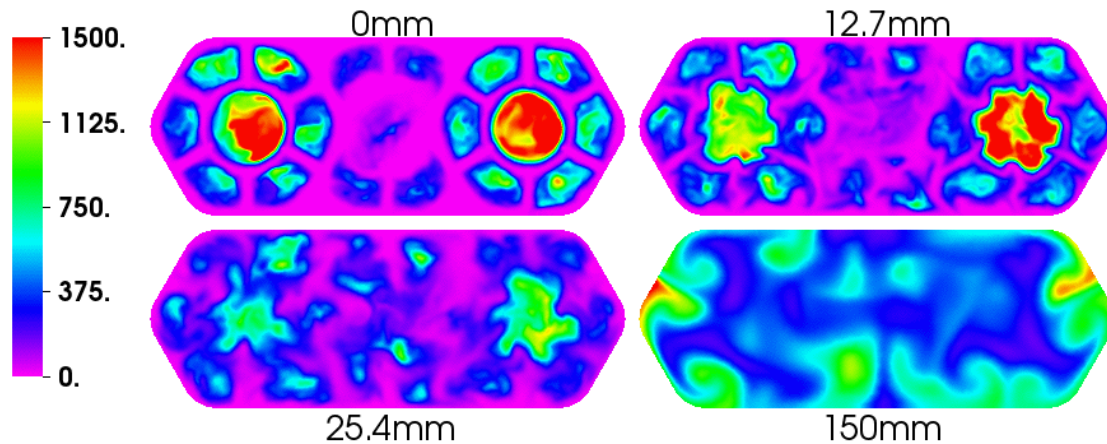
Figure 15a. Contours of NO mass-fraction (*1e6) (NCC **TFNS Reacting** flow): Axial cut at Y-axis mid-plane (left, three pilots and four mains) and Y-axis quarter-plane (right, six mains)

Figure 15b. Contours of NO mass-fraction (*1e6) (NCC **TFNS Reacting** flow): Axial cuts at X-axis mid-planes through three pilots

Figure 16. Contours of NO mass-fraction (*1e6) (NCC **TFNS Reacting** flow): Transverse cuts at combustor dome face (0mm), two downstream planes, exit plane (150mm)

5.0 SUMMARY

The National Combustor Code (NCC) was used to evaluate a nineteen element LDI-3 injector assembly designed by Woodward, FST Inc. Non-reacting flow RANS and TFNS simulations were performed of the LDI-3 configuration consisting of three injection modules – two seven-element modules with six main-injectors (axial air flow, filming-elements) and an integrated pilot injector (radial air flow, axial fuel flow), and one five-element module (four mains and one pilot). Significant differences in the predicted aerodynamic flow structures were observed between the RANS and TFNS simulations. The non-reacting TFNS solution was used to initiate two-phase fuel-air mixing computations with Lagrangian-spray modeling for the liquid phase fuel droplets. Reacting flow computations to evaluate mixer performance and injector behavior were performed using a finite-rate reduced-kinetics model and a PDF turbulence-chemistry interaction model.

The CFD evaluation revealed several unique characteristics of the non-reacting and reacting flow patterns associated with the newly designed pilot swirlers and the pre-filming main injectors. The CFD predicts limited interaction between the central 5-element module with its two adjacent 7-element modules in the first 25mm of the combustor downstream of the dome. The pilot injectors were predicted to produce the majority of the NOx, which could serve to guide possible design refinements for NOx reduction. Some of the modeling lessons learned will be used to reduce the overall computational effort required for the CFD evaluation of the nineteen-element assembly for *multiple* N+3 ICAO power conditions.

6.0 REFERENCES

[1][Tacina 2005] Tacina, R., Lee, P., and Wey, C., "A Lean-Direct-Injection Combustor Using a 9 Point Swirl-Venturi Fuel Injector," ISABE 2005-1106.

[2][Van Zante 2015] Van Zante, Dale E., and Suder, Kenneth L., Environmentally Responsible Aviation: Propulsion Research to Enable Fuel Burn, Noise and Emissions Reduction, International Symposium on Air Breathing Engines (ISABE 2015); 22nd; 25-30 Oct. 2015; Phoenix, AZ

[3][Walton 2015] Walton, J. C., Chang, C. T., Lee, C-M, and Kramer, S., Low NOx Fuel Flexible Combustor Integration Project Overview, NASA/TM-2015-218886.

[4][Reddy 2016] Reddy, D. R. and Lee, C-M, An Overview of Low-Emission Combustion Research at NASA Glenn, ASME Turbo Expo 2016: Turbomachinery Technical Conference and Exposition GT2016; 13-17 Jun. 2016; Seoul S. Korea; Paper GT2016-56100

[5][Goeke 2014] Goeke, J., Pack, S., Zink, G., and Ryon, J., "Multi-Point Combustion System Final Report," NASA/CR-2014-218112, June 2014.

[6][Hicks 2014] Hicks, Y. R. Tedder, S. A., Anderson, R. C., Iannetti, A. C., Smith, L. L. and Dai, Z., NASA Numerical and Experimental Evaluation of UTRC Low Emissions Injector, 50th AIAA/ASME/SAE/ASEE Joint Propulsion Conference, AIAA Propulsion and Energy Forum, Cleveland, OH

[7][He 2015] He, Z. J., Chang, C. T., and Follen, C. E., NOx Emissions Performance and Correlation Equations for a Multipoint LDI Injector, AIAA SciTech 5-9 January 2015, Kissimmee, Florida 53rd AIAA Aerospace Sciences Meeting (AIAA Paper 2015-0098)

[8][Tacina 2016] Tacina, K. M., Podboy, D. P., He, Z. J., Lee, P., Dam, B. and Mongia, H., A Comparison of Three Second-generation Swirl-Venturi Lean Direct Injection Combustor Concepts, 52nd AIAA/SAE/ASEE Joint Propulsion Conference, AIAA Propulsion and Energy Forum, Salt Lake City UT (AIAA 2016-4891)

[9][He 2016] He, Z. J., Wey, C., Chang, C. T., Lee, C-M, Surgenor, A. D., Kopp-Vaughan, K., and Cheung, A., Emission Characteristics of A P&W Axially Staged Sector Combustor, AIAA SciTech 2016; 4-8 Jan. 2016; San Diego, CA, 54th AIAA Aerospace Sciences Meeting.

[10][Herbon 2017} Herbon, J., Aicholtz, J., Hsieh, S-Y, Viars, P., Birmaher, S., Brown, D., Patel, N., Carper, D., Cooper, C., and Fitzgerald, R., N+2 Advanced Low NOx Combustor Technology Final Report, NASA/CR-2017-219410

[11][Ajmani 2013] Ajmani, K., Mongia, H.C. and Lee, P., "CFD Best Practices to Predict NOx, CO and Lean Blowout for Combustor Design," ASME IGTI Paper GT2013-95669, ASME Turbo Expo 2013, San Antonio TX, June 2013.

[12][Ajmani 2014a] Ajmani, K., Mongia, H. C., and Lee, P., "CFD computations of emissions for LDI-2 combustors with simplex and airblast injectors", AIAA Paper 2014-3529, 50th AIAA Joint Propulsion Conference, July 2014.

[13][Ajmani 2014b] Ajmani, K., and Breisacher, K., "Simulations of NOx Emissions from Low Emissions Discrete Jet Injector Combustor Tests", AIAA Paper 2014-3524, 50th AIAA Joint Propulsion Conference, July 2014.

[14][Ashcraft 2011] Ashcraft, Scott W.; Padron, Andres S.; Pascioni, Kyle A.; Stout, Gary W., Jr.; Huff, Dennis L., Review of Propulsion Technologies for N+3 Subsonic Vehicle Concepts, NASA/TM-2011-217239.

[15][Hicks 2016] Hicks, Y. R. Tedder, S. A. and Anderson, R. C., Alternative Bio-Derived JP-8 Class Fuel and JP-8 Fuel: Flame Tube Combustor Test Results Compared using a GE TAPS Injector Configuration AIAA/SAE/ASEE Joint Propulsion Conference; 52nd; 25-27 Jul. 2016; Salt Lake City, UT

[16][Surgenor 2016] Surgenor, A., A Path to N+3 Fuel-Flexible Combustors, Green Aviation Technical Information Meeting, March 31, 2016.

[17][Ajmani 2016] Ajmani, K., Mongia, H.C. and Lee, P., "CFD Based Design of a Filming Injector for N+3 Combustors," AIAA Paper 2016-4783, 52nd AIAA Joint Propulsion Conference, July 2016, Salt Lake City, UT.

[18][Tacina 2017] Tacina, K.M., Podboy, D.P., Lee, P., and Dam, B., "Gaseous Emissions Results from a Three-Cup Flametube Test of a Third-Generation Lean Direct Injection Combustor Concept", ISABE 2017 meeting (to appear).

[19][Ajmani 2015] Ajmani, K., Mongia, H.C. and Lee, P., "Parametric Design of Injectors for LDI-3 Combustors," AIAA Paper 2015-3785, 51st AIAA Joint Propulsion Conference, July 2015, Orlando, FL.

[20][Swanson 1997] Swanson, R.C., and Turkel, E., "Multistage Schemes with Multigrid for Euler and Navier-Stokes Equations," NASA TP-3631, 1997.

[21][Shih 1998] Shih, T.-H., Chen, K.-H., Liu, N.-S., Lumley, J. L., "Modeling of Turbulent Swirling Flows," NASA-TM 1998–113112.

[22][Shih 2000] Shih, T.-H., Povinelli, L.A., Liu, N.-S and Chen, K.-H., "Generalized Wall Function for Complex Turbulent Flows," NASA TM 2000-209936.

[23][Liu 2011] Liu, N.-S., Shih, T.-H. and Wey, C.T., "Numerical Simulations of Two-Phase Reacting Flow in a Single-Element Lean Direct Injection (LDI) Combustor Using NCC," NASA/TM—2011-217031.

[24][Liu 2014] Liu, N.-S., and Wey, C.T., "On the TFNS Subgrid Models for Liquid-Fueled Turbulent Combustion," AIAA Paper 2014-3569, AIAA Propulsion and Energy Conference, Cleveland, OH, July 2014.

[25][Raju 2000] Raju, M.S. and Liu, N.-S., "An Overview of the NCC Spray/Monte-Carlo-PDF Computations", 38th AIAA Aerospace Sciences Meeting, Reno NV (AIAA Paper 2000-0337)

[26][Ajmani 2014c] Ajmani, K., Kundu, K., and Yungster, S., "Evaluation of Reduced Mechanisms for Combustion of Jet-A in LDI Combustor CFD Calculations," AIAA Paper 2014-3662, AIAA Propulsion and Energy Conference, Cleveland, OH, July 2014.

[27][Raju 2012] Raju, M. S., "LSPRAY-IV: A Lagrangian Spray Module," NASA CR-2012-217294.

APPENDIX A

Reduce-Kinetics Model for Finite-Rate Modeling of Jet-A/Air Chemistry

A finite-rate chemistry model was used to compute the species source-terms for Jet-A/air chemistry. Reacting flow computations were performed with the chemical-kinetics model described in Table A1. The chemistry model incorporates 14 species and 18 chemical reaction steps. Jet-A fuel is modeled as a surrogate mixture of decane (73%), benzene (18%) and hexane (9%). The kinetics mechanism was validated by matching adiabatic flame temperature, flame-speed and ignition-delay with experimental shock-tube data in the equivalence ratio range of 0.5 to 1.0, and with experimental data for NO emissions [Ajmani 2014c].

The kinetics model uses **A** (pre-exponential factor), **n** (temperature exponent) and **E** (activation energy, cal/mol) to compute the Arrhenius rate coefficient, $k = A \, (T/T_0)^n \, e^{(-E/RT)}$, for a given temperature, **T** (K). (**R** = universal gas constant, T_0 (K) is a reference temperature). Note that reaction steps 1-3 are irreversible, and reaction steps 4-18 are formulated as reversible reactions. The kinetics for NOx prediction includes an extended Zeldovich mechanism (four steps for NO) and an additional four steps for N_2O species. The inclusion of N_2O is expected to improve the NOx predictions in the small local regions where fuel-rich burning is occurring in the flow. This model was also anchored with LDI-2 experimental data as reported in [Ajmani 2014b] and for LDI-3 parametric design [Ajmani 2015][19], [Ajmani 2016][17] with NCC.

Table A1: Kinetics mechanism for Jet-A fuel surrogate reported in [Ajmani 2014c][26]

	Reaction	A	n	E
1	$C_{11}H_{21} + O_2 => 11CH + 10H +$	1.00E+12	0.00	3.10E+04
	GLO / $C_{11}H_{21}$ 0.8/			
	GLO / O_2 0.8/			
2	$CH + O_2$ $=> CO + OH$	2.00E+15	0.00	3.00E+03
3	$CH + O$ $=> CO + H$	3.00E+12	1.00	0.00E+00
4	$H_2 + O_2$ $<=> H_2O + O$	3.98E+11	1.00	4.80E+04
5	$H_2 + O$ $<=> H + OH$	3.00E+14	0.00	6.00E+03
6	$H + O_2$ $<=> O + OH$	4.00E+14	0.00	1.80E+04
7	$H_2O + O_2$ $<=> 2O + H_2O$	3.17E+12	2.00	1.12E+05
8	$CO + OH$ $<=> CO_2 + H$	5.51E+07	1.27	-7.58E+02
9	$CO + H_2O$ $<=> CO_2 + H_2$	5.50E+04	1.28	-1.00E+03
10	$CO + H_2 + O_2 <=> CO_2 + H_2O$	1.60E+14	1.60	1.80E+04
11	$N + NO$ $<=> N_2 + O$	3.00E+12	0.30	0.00E+00
12	$N + O_2$ $<=> NO + O$	6.40E+09	1.00	3.17E+03
13	$N + OH$ $<=> NO + H$	6.30E+11	0.50	0.00E+00
14	$N + N + M <=> N_2 + M$	2.80E+17	-0.75	0.00E+00
15	$H + N_2O$ $<=> N_2 + OH$	3.50E+14	0.00	7.55E+02
16	$N_2 + O_2 + O <=> N_2O + O_2$	1.00E+15	0.00	3.02E+02
17	$N_2O + O$ $<=> 2NO$	1.50E+15	0.00	3.90E+04
18	$N_2O + M$ $<=> N_2 + O + M$	1.16E+15	0.00	3.32E+04